Coupling single particle ICP-MS with field-flow fractionation for characterizing metal nanoparticles contained in nanoplastic colloids

Angela Barber, Sun Kly, Matthew G. Moffitt, Logan Rand, & James F. Ranville

January 2020

Coupling Single Particle ICP-MS with Field-flow Fractionation for Characterizing Metal Nanoparticles Contained in Microplastic Colloids

Angela Barber[1,3], Sun Kly[2], Matthew G. Moffitt[2], Logan Rand[1], and James F. Ranville [1*]

[1]Department of Chemistry, Colorado School of Mines, Golden, CO, 80403

[2]Department of Chemistry, University of Victoria, Victoria, B.C. V8W 2Y2

[3]Arcadis U.S., Inc., Broomfield, CO, 80021

KEYWORDS: *Centrifugal FFF, AF4, polymer nanocomposite, nanotechnology, heteroaggregates*

ABSTRACT: Use of nano-enabled products increases the potential for release of engineered nanoparticles (ENP) into the environment. Product weathering and further environmental transformations can create composite particles (CPs) that may contain multiple ENPs, a residual product matrix, or transformed/added surface coatings. Methodology that uses transmission electron microscopy (TEM), single particle ICP-MS (spICP-MS) and field-flow fractionation (FFF) was developed to facilitate the investigation of metallic ENPs associated with CPs. In this study, colloidal-sized microplastic CPs consisting of gold-polymer nanocomposite (polystyrene-*block*-poly(acrylic acid)) were examined to reveal how combining FFF with spICP-MS can be used to characterize CPs. Metal NP size and particle number concentration is obtained by spICP-MS. Asymmetric flow field-flow fractionation (AF4) and centrifugal field-flow fractionation (CFFF) separate and size the CPs based on their hydrodynamic diameter and buoyant mass, respectively. Off-line spICP-MS analysis of fractions obtained by the FFF separations facilitated measurement of the mass and number of Au-PS (gold-polystyrene) ENPs (from 1 to >8) contained in the CPs. In particular, CFFF utilizing a carrier that was density-matched to the polymer proved very successful in measuring multiple gold ENPS in the CPs. The developed methodology can be applied to investigate ENP properties in environmental systems and to facilitate the use of embedding metal NPs into microplastic CPs in order to track their environmental transformations.

INTRODUCTION

The uncertainty over the possible consequences of introducing engineered nanoparticles (ENPs) and microplastics (MPs) into the environment is a driver to develop new analytical methods for their characterization. ENPs are incorporated into nanotechnology-enabled products in order to provide a desired function, resulting in large societal benefits[1]. Similarly, the key role plastics play in society has led to the environmental release of MPs. Predicting the risks posed to human health and the environment by these materials is difficult due to challenges in quantifying exposure parameters (e.g., release rates, transport, stability, and fate). Among the unknowns is the form of released ENPs. Partial transformations can occur in the environment through surface modification (i.e. formation and alteration of coatings), hetero-aggregation with natural particles, and partial chemical degradation (e.g. surface oxidation or sulfidation)[2,3]. Environmental samples may therefore commonly contain ENPs existing in a complex composite structure (i.e. multielement, multiphase). It has been recently proposed that the environmental behavior of MPs could be better examined by introducing metals into the polymer [4]. Using metal NPs could be similarly useful, with the added benefit that each NP has a well-known elemental mass. Embedding even a single NP into each MP can introduce a substantial number of metal ions. Clearly there is a need for continued advancements in nanometrology capable of analyzing increasingly complex materials[4-6].

This study focused on new combinations of analytical approaches capable of characterizing composite particles (CPs) that contain both metallic and organic (polymeric) phases, which can represent ENP-containing materials likely to be found in the environment. Protein coronas formed on ENPs during biological interaction/uptake[11-13] and colloidal-sized MP fragments (e.g., polymer-NP composites) generated by weathering of nano-enabled products are examples. In this latter case the fragments could

retain some of their polymer matrix[14] and have a structure consisting of one or more inorganic NPs incorporated inside colloidal MPs. In environmental systems, CPs having both organic and inorganic components are likely to be created due to the ubiquity of natural background mineral particles, dissolved organic matter (i.e., humic substances), and biomolecules. In this study Au NPs contained in polymer core/shell colloids were prepared and characterized to represent these CP types.

The development of new nanometrology to quantify (mass and/or number concentration) and characterize (size, composition, structure, aggregation state) colloids, including ENPs, is essential to assessing the impacts of their release[15]. Quantitative characterization of complex CPs by traditional nanometrology techniques, such as transmission electron microscopy (TEM) and dynamic light scattering (DLS), is often challenging and prone to artifacts[16,17]. To address this issue, we present an analytical methodology using single particle ICP-MS (spICP-MS) applied following a separation step, in this case field-flow fractionation (FFF). This combination of techniques is a highly promising alternative and/or addition to the traditional techniques to more fully characterize CPs. The methods can provide the total CP size, the number of NPs per CP, and the thickness of the organic/polymer coating. Analysis by spICP-MS provides the particle number concentration and the inorganic NP size, which is based on elemental mass[18-22]. Asymmetrical flow field-flow fractionation (AF4) and centrifugal FFF (CFFF) separate the sample constituents based on their hydrodynamic size and buoyant mass, respectively[23-24]. FFF theory or size calibration can be used to compute particle size.

The first study objective was to compare the techniques of TEM, spICP-MS, AF4, and CFFF for measuring mean size and size distribution width of monodisperse ENPs. The second objective was to demonstrate the quantitative capabilities of spICP-MS for characterizing CPs that may contain multiple NPs. A key parameter obtained by the spICP-MS methodology is the particle size distribution width, as this measurement can be a sensitive indicator of aggregation. We demonstrate that increased size distribution width determined by spICP-MS can show the presence of CPs containing multiple metal NPs.

The third objective of this study was to determine the distribution of metal NPs incorporated in CPs as size or buoyant mass increases. Within the third objective, we show: 1.) FFF provides information on how multiple NPs are distributed across the size distribution and 2.) CFFF can provide separation of CPs by the number of metal NPs contained therein. The methodologies developed in this project overcomes some key limitations in other techniques, and has potential use in industrial manufacturing processes, monitoring release of ENPs and MPs into the environment, and assessing abiotic and biologically-mediated transformations of these materials.

MATERIALS AND METHODS

Model Composite Particle Synthesis. The model CP used was a polymer nanocomposite (Au-PS/PS-*b*-PAA) that could contain none, one, or many of the precursor Au-PS NPs (Figure 1). Polystyrene brush-coated Au NPs (Au-PS) were first prepared by coating Au-citrate precursor NPs (Au-cit, approximately 40-50 nm in diameter). Water-dispersible CPs were created using amphiphilic block copolymer polystyrene-block-poly(acrylic acid) (PS-*b*-PAA) chains, which form a coating up to about 200 nm thick (Figure 1). Dispersions of Au-PS/PS-*b*-PAA CPs were prepared by microprecipitation of Au-PS NPs and the amphiphilic block copolymer PS-*b*-PAA dispersed in dimethylformamide via mixing with water in a two-phase gas-liquid microfluidic reactor. Details of the microfluidic reactor and its application to producing polymer-inorganic CPs can be found in previous publications [26-29]. Specific details of the synthesis of both the precursor Au-PS NP and the CP are provided in the ESI (ESI-1 and ESI-2).

Characterization Methods. All materials were analyzed by spICP-MS, AF4, CFFF, and TEM. Total ^{197}Au concentrations of the solutions containing Au-cit NP and Au-PS/PS-*b*-PAA CP colloids (1:1000 dilution in Milli-Q water) were measured by ICP-MS (Perkin Elmer NexION 300D) using a dwell time of 2.19 seconds (matching AF4-UV-vis data collection frequency) with 55 total readings and

a 1 mL/min sample flow rate. Calibration was performed using 0, 1, 10, and 100 µg/L dissolved Au (SPEX CertiPrep) in 2% (v/v) HCl (Figure ESI-1).

TEM imaging of the Au-cit precursor NPs and the Au-PS/PS-*b*-PAA CPs was conducted using Jeol JEM 1400 operated at 80 keV. Samples were dropped onto CF300-Cu Carbon film mesh copper grids from deionized water and whisked dry after 30 seconds. To minimize beam damage, low electron voltages were used and images were collected with a bottom-mounted Gatan SC200 CCD camera. ImageJ™ image analysis software was used to evaluate particle distributions.

The Au-cit NPs and the Au-PS/PS-*b*-PAA CPs were also analyzed by spICP-MS. Additionally, during separation by AF4 and CFFF, selected fractions of the eluent were collected, diluted, and analyzed by spICP-MS. Analyses were performed using 100 microsecond (µs) dwell times, no settling time, and a very short detector dead time (35 ns) between readings[30-32]. Additional acquisition conditions and a summary of all spICP-MS analyses performed are shown in the ESI (Table ESI-1, ESI-2). Data acquisition and data processing were performed using a pre-release version of the Syngistix™ Nano Application Module provided to the authors by Perkin Elmer. A 60 nm Au NP (NIST SRM 8013) and dissolved Au standards were used to determine spICP-MS transport efficiency following the mass-based procedure of Pace et al.[33] and was typically 6-12%. Particle events were identified as ICP-MS responses above the threshold intensity, determined using the average plus 3σ method[33]. The total intensity of each NP event is determined by summation of all consecutive readings above the threshold, from which the element mass is determined and particle diameter is computed assuming a spherical geometry and a gold density of 19.3 g/cm^3. The particle number concentration is proportional to the number of NP events detected after adjustment for the sample flow rate and transport efficiency.

A Postnova Analytics AF2000 AT AF4 with online UV-visible (254 and 520 nm wavelengths) and/or ICP-MS detectors was used to separate, by hydrodynamic size, the Au-cit NPs and Au-PS/PS-*b*-PAA CPs. All separations were performed with a cross-flow of 0.5 mL/min and an outlet flow rate of 1

mL/min to the detector(s). Other specific details of the FFF separation conditions and the measurement of the percent recovery are provided in the ESI (Table ESI-3). Hydrodynamic diameter was calibrated using dispersions of 0.01% (v/v) PS spheres of 60 nm, 100 nm, and 140 nm (Thermo Scientific) and/or 30 nm and 60 nm Au-citrate NPs (NIST, SRM 8012 and SRM 8013, respectively) (each at 1.25-12.5 mg/L). Size calibrations were performed at least once each day of AF4 analysis (Figure ESI-2). On-line ICP-MS also provided a continuous fractogram for ^{197}Au. Several separations of the Au-PS/PS-*b*-PAA CPs are reported, as summarized in Table ESI-3.

A Postnova Analytics CF2000 CFFF was used to separate and size the precursor Au-cit NPs and the Au-PS/PS-*b*-PAA CPs. For the latter, a carrier solution of 24% (v/v) glycerol and 0.05% (v/v) FL-70 was used. This provided a density of approximately 1.056 g/mL, which closely matched the density of the PS-*b*-PAA shell (assumed to be 1.05 g/cm^3). The resulting neutral buoyancy of the polymer coating provided separation by the incorporated Au mass only. A power decay program was used, which provided a non-linear relationship between retention time and particle mass. Thirty fractions (3 minutes duration) were collected, and select fractions were analyzed by spICP-MS. Online UV-vis (Postnova Analytics) at 254 nm and 520 nm and/or 90° light scattering detectors (Postnova Analytics) were used to monitor sample elution. A summary of each separation is provided in the ESI (Table ESI-3). All NP samples, size standards, and FFF fractions were stored at 4°C and diluted in Milli-Q water (18.2 MΩ-cm) each day. Diluted NPs were sonicated for 5 minutes following preparation.

RESULTS AND DISCUSSION

Comparison of Size Analysis Methods for Low-Polydispersity NPs. The size distributions of the precursor Au-cit NPs were determined by spICP-MS, AF4, and CFFF. Incorporation of multiple Au NPs into CPs (polymer-NP or heteroaggregates) increases both the mean size and the size distribution

144 width (polydispersity) compared to the original (precursor) Au NP population. In applying spICP-MS to
145 characterize these complex particles using these metrics, it is important to know the comparability to
146 results obtained by other methods. For inorganic, monodisperse particles the most-widely accepted
147 standard for comparison is TEM, which was used to examine the Au-PS precursor NP and the CP. TEM
148 images of the Au-PS NP precursors (Figure 1a,c) show relatively uniform but somewhat pill-shaped
149 particles. The equivalent spherical diameter was computed from the volume obtained by:

150 $$V = 4/3\ \boldsymbol{\pi}(P_t)^3 + \boldsymbol{\pi}(P_d)^2\ P_h \qquad (1)$$

151 Where: P_h = length of the cylindrical portion, P_d = short dimension of the cylindrical portion, and P_t =
152 the length of the hemispherical ends of the pill. ImageJ™ particle distribution analysis was applied to 222
153 particles. The PS coating was not imaged by this method, allowing comparison of the size results to that
154 obtained by other methods for the Au-cit NPs.

155 Particle size distributions obtained for the precursor NPs by the four methods are shown in Figure
156 2 (a-d). Mass of the Au-cit NPs obtained by spICP-MS was converted to an equivalent spherical diameter
157 using an Au density of 19.5 g/cm^3. AF4 and CFFF size distributions were obtained from retention time
158 by calibration. Nanoparticle size distributions were fitted to Gaussian and LogNormal non-linear curve
159 functions using OriginPro 2018™. The fitting parameters μ (mean size) and σ (distribution width) along
160 with their respective standard error reported by the software are shown in Table 1. The error is a measure
161 overall fit of the data by the gaussian and log normal models.
162

Table 1. Gaussian and Log-Normal fitting statistics of size distributions for Au-PS NP size determined via TEM and Au-cit NP determined by spICP-MS, AF4, and CFFF. Degrees of freedom (DF) represent the number of histogram bins.

Equivalent spherical diameter (nm)		**TEM**		**spICP-MS**		**AF4**		**CFFF**	
		value	error	value	error	value	error	value	error
Gaussian	μ	46.8	0.52	39.8	0.13	45.4	0.04	41.4	0.02
	σ	7.0	0.82	6.4	0.19	7.3	0.04	4.6	0.02
	DF	17		49		298		702	
	RSS	0.215		0.106		0.193		0.715	
Log Normal	μ	47.6	0.62	40.7	0.20	46.4	0.03	41.8	0.03
	σ	7.2	0.94	6.4	0.31	7.7	0.03	4.6	0.04
	DF	17		49		298		702	
	RSS	0.210		0.215		0.082		1.83	

In the comparison of the four different particle sizing methods, all Gaussian and LogNormal models report similar μ and σ values as well as error (adjusted r^2) for the particle size distributions. The Au-cit NP distribution width obtained by spICP-MS is consistent with TEM results; however, the mean diameter calculated by TEM is about 15% greater than the spICP-MS diameter. AF4-ICP-MS and CFFF-UV-vis results are more consistent with the spICP-MS results. Overall, all four of the methods appeared to give mean sizes within approximately 10% regardless of the distribution model used. The residual sum of squares is minimized slightly more by the Gaussian model for spICP-MS and the LogNormal model for the AF4 data. The CFFF data did not seem to fit either model well as shown by the higher residual sum of squares. These results support the hypothesis that the distribution width obtained by spICP-MS is comparable to TEM and that this measurand can be used to examine the characteristics of the CPs generated in this study. Additional comparisons of spICP-MS and TEM (Figure ESI-3) were made for

other NP reference materials (NIST RM 8013, Nanocomposix NPs) or varying distribution width. The result further support the observation that TEM and spICP-MS give comparable distribution widths.

Table 2. Gaussian and Log Normal fitting statistics on Au-cit NP and Au-PS-*b*-PAA NP mass distributions. Degrees of freedom (DF) represent the number of mass bins.

Mass in μg Au × 10^{-9}		**Au-Citrate Mass**		**Au-PS-b-PAA Mass**	
		value	standard error	value	standard error
Gaussian	μ	0.71	0.01	1.53	0.02
	σ	0.30	0.01	0.52	0.02
	DF	46		198	
	RSS	0.193		1.319	
Log Normal	μ	0.84	0.024	1.81	0.02
	σ	0.41	0.032	0.79	0.02
	DF	46		198	
	RSS	0.213		0.554	

Characterization of CPs by spICP-MS Analysis. TEM analysis of the CPs shows Au-PS NPs incorporated inside the larger CPs (Figure 1d). A wide variation in the number of Au NPs per CP was observed by TEM image processing (ImageJ™). Many polymer particles were observed to contain no Au NPs, but for those that did contain Au NPs, almost 50% contained only one Au NP, about 30% contained two or three Au NPs, and the remaining 20% had four or more Au NPs. However we observed that in some cases it appeared that NP overlap could result in an overestimate of the number of single particles in the CP.

Examining mass distributions obtained by spICP-MS (Figure 3), instead of the size distribution, allows for a clearer analysis of the number of NPs incorporated into the CPs. Mass distributions were fitted to Gaussian and LogNormal non-linear curve functions using OriginPro 2018™. The fitting

parameters μ (mean size) and σ (distribution width) along with their respective standard errors reported by the software are shown in Table 2. The mass distribution of the precursor Au-cit NPs is fit slightly better by a Gaussian distribution than a LogNormal distribution (as shown by the residual sum of squares). This is in contrast to the Au-PS/PS-*b*-PAA CPs, which are much more closely fit by a LogNormal mass distribution. The skewed Au mass (size) distribution clearly indicates incorporation of multiple Au NPs into the CPs, as was visually observed by TEM. The mean Au mass (1.53×10^{-9} μg Au) is slightly larger than twice that of the precursor mass (0.71×10^{-9} μg Au). This result suggests that most CPs contain 2 NPs with 1 and 3 NPs being the next most common. The discrepancy between this spICP-MS and the TEM result may be attributed to a bias resulting from the overlap of multiple three-dimensional Au NPs in the two-dimensional TEM images, along with poorer counting statistics by TEM.

Using multiples of the Au-cit NP mode mass, it can be seen that the tail of the distribution indicates CPs contain progressively fewer multiple NPs up to approximately 10 NPs. Addition of two FFF techniques, AF4 and CFFF, to the spICP-MS and TEM data provides a more complete particle characterization for CPs by coupling CP particle separation based on hydrodynamic size or density with single particle Au NP mass analysis.

Characterization of CPs by Field-Flow Fractionation w/spICP-MS Analysis. The Au-PS/PS-*b*-PAA CPs and the Au-cit NP precursors were separated by both AF4 (Figure 4) and CFFF (Figure 5). Analysis of fractions collected during both methods of separation by spICP-MS provides mass distributions of Au NPs at various retention times. To provide an approximation of the number of Au NPs observed within each FFF fraction, the spICP-MS mean mass of the Au-cit NPs (0.71×10^{-9} μg Au) was used to develop simplified stacked bar histograms (Figure 4b and 5b). To produce these stacked bar histograms, the midpoint between the mean mass multiplied by an integer value of 1 to 8 was found. The number of particles (i.e., frequency) between each midpoint was summed and combined to determine an approximate Au NP number distribution in each fraction. For example, to find the number of CPs

containing the equivalent mass of three Au NPs, the frequency of particles between a mass of 1.86×10^{-9} μg and 2.60×10^{-9} μg was summed and normalized to the total frequency. This was performed for up to 8 NPs for both the Au-cit NP and Au-PS/PS-*b*-PAA CP spICP-MS data.

Asymmetric Flow Field-Flow Fractionation. The AF4 recovery for Au-cit and Au-PS/PS-b-PAA CPs was calculated as the total integrated intensity over the fractogram (Figure 2c and 4a) with a field applied (0.5 mL/min cross-flow) divided by the integrated intensity of the fractogram with no field applied (0 mL/min cross-flow). Total average recovery was 82% and 127%, for Au-cit and Au-PS/PS-b-PAA CPs, respectively (Figure ESI-4). These recoveries were considered acceptable, but not ideal. The recoveries indicate possible interaction of the CPs with the membrane. The low recovery may be indicative of irreversible adsorption. Some CPs appear to be reversibly adsorbed as demonstrated by the peak that elutes after the field is turned off at the end of the fractionation (90 minutes in Figure 4a). When ignoring this peak the recovery drops to 70% and 85% for the Au-cit and Au-PS/PS-b-PAA CPs respectively.

Two-minute duration fractions were collected during AF4 separation of the Au-PS/PS-*b*-PAA CP, and select fractions were analyzed for ^{197}Au by spICP-MS (Figure 4b). All fractions were analyzed at a 1:10 dilution factor. In addition to the AF4 separations for which fractions were collected and recovery was determined, two additional replicate separations were performed under the same conditions. A comparison of the peak maxima elution time for the various fractograms (Figure ESI-5) shows good reproducibility with an elution time of 22 ± 2.1 minutes (mean ± standard deviation) and a range from 19.4 minutes to 25.4 minutes. Four fractions were analyzed by spICP-MS for ^{197}Au (Figure 4a, Table ESI-2). Hydrodynamic diameter for each fraction was computed as 70-87 nm, 175-193 nm, 245-263 nm, and 386-403 nm. The approximate number of CPs counted for each fraction is as follows: 950 for 70-87 nm, 5100 for 175-193 nm, 3500 for 245-263 nm, and 1500 for 386-403 nm. The spICP-MS mass distributions shift to larger masses as the hydrodynamic diameter increases, which indicates that greater numbers of

Au NPs are incorporated into the larger CPs. The increase in mean Au mass with increasing hydrodynamic diameter supports this observation; however, the mode Au mass does not change significantly, indicating that the CPs most frequently contain a single Au NP. Stacked bar histograms for the various CP fractions were produced from the spICP-MS mass distributions (Figure 4b). A decrease in the fraction of CPs containing 1-2 Au NPs (Figure 4b, yellow and orange bands) and a corresponding increase in the fraction containing ≥8 Au NPs (Figure 4b, black bands) as the CP hydrodynamic diameter increases is evident.

These AF4 results provide distribution of hydrodynamic diameters for the CPs coupled with a distribution of the incorporated Au masses as a function of hydrodynamic size. While the maximum number of possible Au NPs increases as hydrodynamic diameter increases, there is no limit to the minimum number of incorporated Au NPs (i.e., a CP 400 nm in diameter may contain anywhere from zero to over eight Au NPs). As a result, a broad range in the number of incorporated Au NPs is observed at high retention times/large CP hydrodynamic diameters (Figure 4b).

Centrifugal Field-Flow Fractionation. The addition of CFFF to this methodology provides separation of the Au-PS/PS-*b*-PAA CPs based on buoyant Au mass within each CP, and therefore only allows CPs containing multiple Au NPs to be eluted at higher retention times. This is accomplished by matching the carrier density to that estimated for the polymers (1.056 g/cm^3). Online UV-vis (520 nm and 254 nm detection wavelengths) and 90° light scattering detectors were used (Figure ESI-6a,b)Thirty fractions (3 minutes, 1.5 mL each) were collected across the Au-PS/PS-*b*-PAA CP CFFF fractogram, and select fractions were analyzed by spICP-MS for ^{197}Au (Figure 5a, Table ESI-2). CPs not containing Au and any particles that were not focused should elute first in the void peak. Following the void peak, CPs should elute from low to high mass of incorporated Au. The hydrodynamic diameter should not correlate with the Au mass, except for any uncoated Au-PS NP precursors. For example, one Au NP can be incorporated into a CP with a hydrodynamic diameter of 70 nm or of 400 nm, and both would elute before

CPs containing two Au NPs. The effective Au mass was also calculated from the CFFF retention times based on FFF theory[23,24] (Figure ESI-6c).

Of the 16 CFFF fractions analyzed by spICP-MS, results for fractions 10, 15, 20, 25, and 30 are shown in Figure 5. The approximate number of CPs counted for each fraction is as follows: CFFF 10 = 5300, CFFF 15 = 5600, CFFF 20 = 6000, CFFF 25 = 5700, and CFFF 30 = 5100. There is an overall trend from low to high number of incorporated Au in these fractions. Particle numbers were very low for the final fraction (30) and slight carryover of NPs that are slowly being released from the membrane might explain the presence of a broader range of Au NP numbers. The other CFFF fractions were analyzed approximately 9 weeks after the first set (17, 18, 22, 23, 27, and 28) and the observations slightly disrupt this trend, particularly in fractions 17 and 18 (Figure ESI-7, Figure ESI-8). These two fractions show a much higher fraction of particles with large Au mass and have a lower concentration of NPs compared to the surrounding fractions (15 and 20). It is likely that the extended sample storage led to particle aggregation, indicating that spICP-MS analysis should be performed at the time of FFF separation.

Comparison of these results to the expected effective Au mass provided by FFF theory (Figure ESI-6c) shows agreement with the exponential trend. The exponential increase in the effective Au mass (due to the CFFF power decay program used for separation) resulted in difficulty resolving the increase in incorporated number of Au NPs at high Au masses (i.e., high retention times). Here, better mass resolution is provided at lower retention times. Future work could refine the CFFF method to obtain better Au mass resolution at large retention times (i.e., a linear increase in effective Au mass); however, such a separation would be time-consuming (> 90 minutes).

CONCLUSION

292 The physical form of ENMs released from products during the use and disposal phase will likely
293 influence their environmental fate and impact. We have shown that using multiple means of nanoparticle
294 characterization provides a clearer picture of the physical properties (i.e. size, number of incorporated
295 components) of released ENMs. Given the good agreement in size distributions obtained by TEM and
296 spICP-MS for monodisperse NPs, the increase in size distributions caused by incorporation of multiple
297 NPs into a larger CP can be measured accurately by spICP-MS. Also, estimates of NP mass by spICP-
298 MS are not influenced by assumptions about NP shape as is the case for TEM. Combining spICP-MS
299 with AF4 provides measurement of both the hydrodynamic diameter of CPs and the mass (size)
300 distribution of the NPs contained in each CP size fraction. Differences in the two size distributions can be
301 used to further characterize CPs. In this case we could rapidly and quantitatively measure the number of
302 Au NPs contained in differently sized CPs. In this study, the results showed that as hydrodynamic diameter
303 increased, the range in the number of Au NPs increased, from 0 to > 8. Quantitatively obtaining this
304 information by TEM would be far more difficult. Finally, the application of spICP-MS to CFFF fractions,
305 obtained using a carrier solution matching the CP polymer density, provided a means of separating the
306 sample as a function of the number of Au-NPs contained in the CP, thus providing a better examination
307 of the incorporation of multiple NPs into larger CP colloids. Application of this approach for other
308 samples containing both organic and inorganic components will require further investigation of how
309 closely the organic matter density must be matched. Although the developed methods are discussed in the
310 context of further investigating the environmental behavior of ENMs, these techniques have obvious
311 applications for materials science (e.g. polymer-nanoparticle composites) and biology (e.g. protein corona
312 formation). A more uniform incorporation of inorganic NPs into MP colloids could provide a precise
313 means of following transformation of MPs including fragmentation and aggregation.

314

315 **ASSOCIATED CONTENT**

Supporting Information

The Supporting Information is available free of charge on the ACS Publications website.

ESI sections ESI-1 to ESI-4 and Tables ESI-1 to ESI-3 provide additional information of particle synthesis and spICP-MS and FFF analysis procedures and equipment. Figures ESI-1 to ESI 8 provide additional experimental results.

AUTHOR INFORMATION

Corresponding Author

* Email:jranvill@mines.edu

ACKNOWLEDGMENT

This study was partially funded by the National Science Foundation (CBET1336168) and the US Environmental Protection Agency through the STAR program (RD83558001). SK and MGM thank the Natural Sciences and Engineering Research Council (NSERC, Canada) for funding. Any opinions, findings, and conclusions or recommendations expressed in this material are those of the author(s) and do not necessarily reflect the views of the NSF and USEPA. The authors wish to thank Dr Soheyl Tadjiki and Dr Robert Reed of Postnova LLC, Salt Lake City for performing the CFFF separations; Mr David Garcia of NanoComposix for providing the Au NP samples of various distribution widths.

REFERENCES

[1] *National Nanotechnology Initiative* Website; Benefits and Applications, http://www.nano.gov/you/nanotechnology-benefits, Accessed 12 September 2016.

[2] Lowry, G.V.; Gregory, K.B.; Apte, S.C.; Lead, J.R. *Environ. Sci. Technol*. **2012**, *46*, 6893−6899.

[3] Mitrano, D.M.; Motellier, S.; Clavaguera, S.; Nowack, B. *Environment International* **2015**, *77*, 132–147.

[4] Klaine, S.J.; Alvarez, P.J.J.; Batley, G.E.; Fernandes, T.F.; Handy, R.D.; Lyon, D.Y.; Mahendra, S.; McLaughlin, M.J.; Lead, J.R. *Environ. Toxicol. Chem.* **2008**, *27*, 1825–1851.

[5] Nowack, B.; Baalousha, M.; Bornhöft, N.; Chaudhry, Q.; Cornelis, G.; Cotterill, J.; Gondikas, A.; Martin Hassellöv, M.; Lead, J.; Mitrano, D.M.; von der Kammer, F.; Wontner-Smith, T. *Environ.Sci.:Nano.* **2015**, *2*, 421–428.

[6] *Progress Review on the Coordinated Implementation of the National Nanotechnology Initiative 2011 Environmental, Health, and Safety Research Strategy*; National Science and Technology Council Committee on Technology, Subcommittee on Nanoscale Science, Engineering, and Technology; June 2014

[7] Hotze, E.M.; Phenrat, T.; Lowry, G.V. *J. Environ. Qual.* **2010**, *39*, 1909–1924.

[8] Zhou, D.; Abdel-Fattah, A.I.; Keller, A.A. *Environ. Sci. Technol.* **2012**, *46*, 7520−7526.

[9] Labille, J.; Harns, C.; Bottero, J-V.; Brant, J. *Environ. Sci. Technol.* **2015**, *49*, 6608−6616.

[10] Wang, H.; Dong, Y.; Zhu, M.; Li, X.; Keller, A.A.; Wang, T.; Li, F. *Water Research*, **2015**, *80*, 130-138.

[11] Lynch, I.; Cedervall, T.; Lundqvist, M.; Cabaleiro-Lago, C.; Linse, S.; Dawson, K.A. *Advances in Colloid and Interface Science*, **2007**, *134–135*, 167–174.

[12] Lundqvist, M.; Stigler, J.; Elia, G.; Lynch, I.; Cedervall, T.; Dawson, K.A. *PNAS,* **2008**, *105*, 14265–14270.

[13] Lundqvist, M.; Stigler, J.; Cedervall, T.; Bergga, T.; Flanagan, M.B.; Lynch, I.; Elia, G.; Dawson, K. *ACS Nano*, **2011**, *5*, 7503-7509.

[14] Duncan, T.V. ACS Appl. Mater. Interfaces **2015**, *7*, 20−39.

[15] *National Nanotechnology Initiative* Website; Environmental, Health, and Safety Issues, http://www.nano.gov/you/environmental-health-safety, Accessed 12 September 2016.

[16] Domingos, R.F.; Baalousha, M.A.; Ju-Nam, Y.; Reid, M.M.; Tufenkji, N.; Lead, J.R.; Leppard, G.G.; Wilkinson, K.J. *Environ. Sci. Technol.* **2009**, *43*, 7277–7284.

[17] Laborda, F.; Bolea, E.; Cepria, G.; Gomez, M.T.; Jimenez, M.S.; Perez-Arantegui, J.; Castillo, J.R. *Analytica Chimica Acta* **2016**, *904*, 10-32.

[18] Degueldre, C.; Favarger, P.Y. *Colloids and Surfaces A: Physicochemical and Engineering Aspects* **2003**, *217* (1), 137-142.

[19] Degueldre, C.; Favarger, P.Y. *Talanta* **2004**, *62* (5), 1051-1054.

[20] Degueldre, C.; Favarger, P.Y.; Bitea, C. *Analytica Chimica Acta* **2004**, *518* (1), 137-142.

[21] Degueldre, C.; Favarger, P.Y.; Rosse, R.; Wold, S. Uranium colloid analysis by single particle inductively coupled plasma-mass spectrometry. *Talanta* **2006**, *68* (3), 623-8.

[22] Degueldre, C.; Favarger, P.Y.; Wold, S. *Analytica Chimica Acta* **2006**, *555* (2), 263-268.

[23] Giddings, J.C. *Science* **1993**, *260* (5113), 1456-1465.

[24] Giddings, J.C. *Anal. Chem.* **1995**, *67* (19), 592A–598A.

[25] Pol, V.G.; Srivastava, D.N.; Palchik,O.; Palchik, V.; Slifkin, M.A.; Weiss, A.M.; Gedanken, A. *Langmuir* **2002**, *18*, 3352-3357.

[26] Wang, C-W.; Oskooei, A.; Sinton, D.; Moffitt, M.G. *Langmuir* **2010**, *26*, 716–723.

[27] Schabas, G.; Wang, C.-W.; Oskooei, A.; Yusuf, H.; Moffitt, M. G.; Sinton, D. *Langmuir*, **2008**, *24*, 10596-10603.

[28] Frens, G. *Nature Physical Science* **1973**, *241*, 20-22.

[29] Rucareanu, S.; Maccarini, M.; Shepherd, J.L.; Lennox, R.B. *J. Mater. Chem.* **2008**, *18*, 5830–5834.

[30] Montaño, M.D.; Badiei, H.R.; S. Bazargan, S.; Ranville, J.F. *Environ. Sci.: Nano* **2014**, *1* (4), 338-346.

[31] Hineman, A.; Stephan, C. *J. Anal. At. Spectrom*. **2014**, *29*, 1252–1257.

[32] Strenge, I.; Engelhard, C. *J. Anal. At. Spectrom.* **2015**, Communication, DOI:10.1039/c5ja00177c.

[33] Pace, H.E.; Rogers, N.J.; Jarolimek, C.; Coleman, V.A.; Higgins, C.P.; Ranville, J.F. *Anal Chem*. **2011,** *83* (24), 9361-9369.

[34] Montaño, M.D.; Olesik, J.W.; Barber, A.G; Challis, K.; Ranville, J.F. Anal Bioanal Chem. **2016**, 408,19, 5053-5074.

[35] Montoro Bustos, A.R.; Petersen, E.J.; Possolo, A.; Winchester, M.R. *Anal. Chem.* **2015**, *87*, 8809−8817.

FIGURES

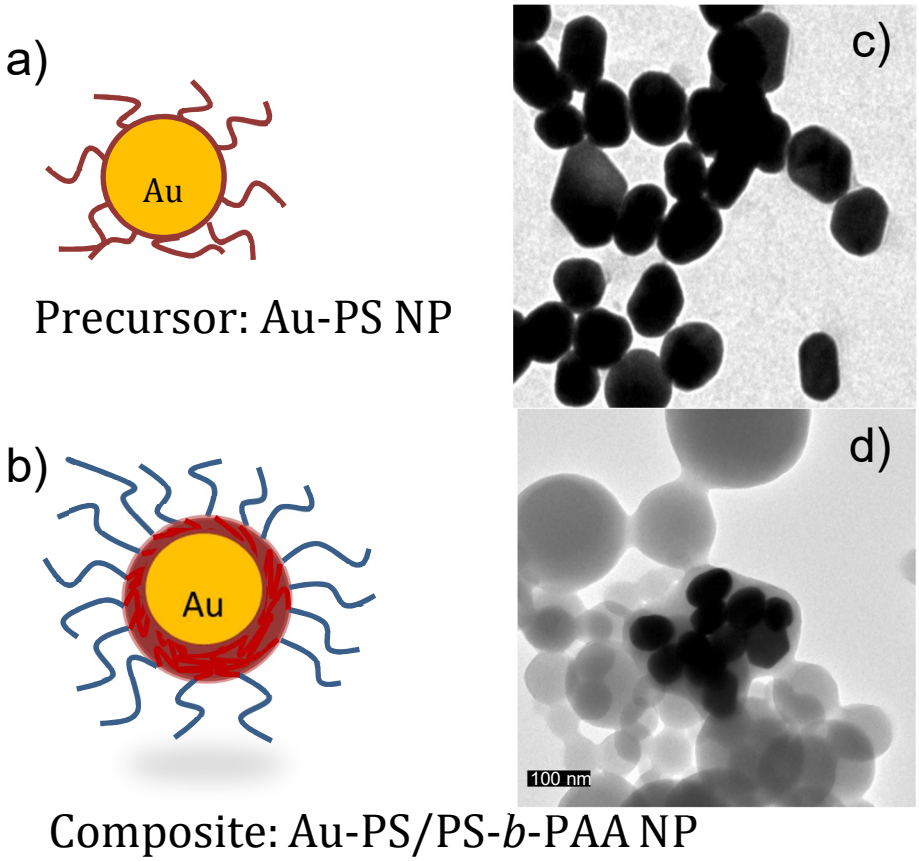

Figure 1. Schematics of a) precursor Au-PS NP and b) Au-PS/PS-b-PAA composite particle. TEM micrographs of c) precursor Au-PS NP and d) Au-PS/PS-b-PAA composite particle. Figure d.) shows one of the CPs having a high number of Au NPs.

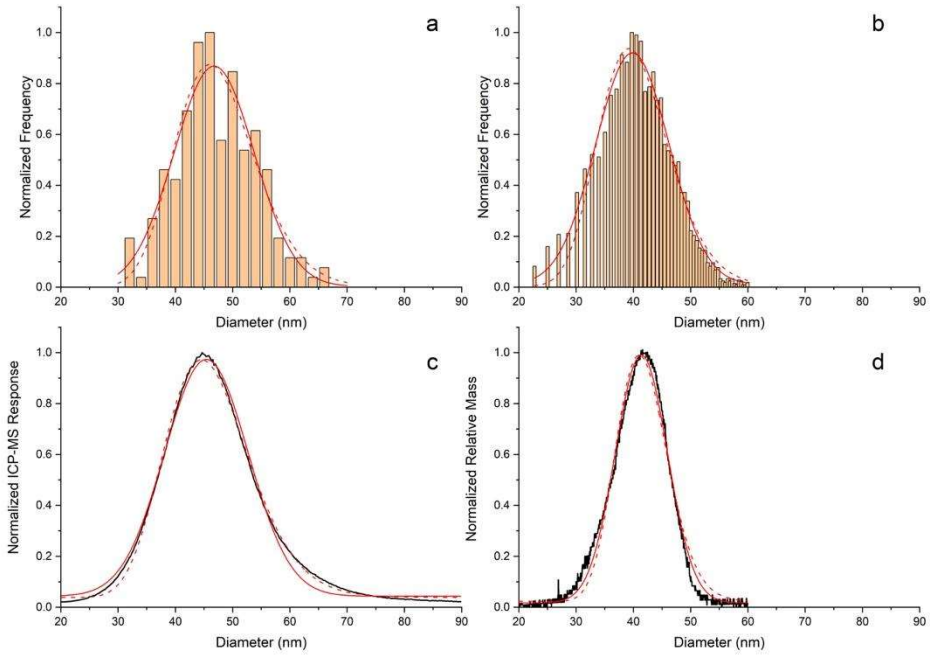

421
422 **Figure 2.** Particle size distributions of the precursor Au-PS NP obtained by a.) TEM, and precursor Au-
423 cit by b.) sp-ICP-MS, c.) AF4, and d.) CFFF. Nanoparticle size distributions were fitted to Gaussian
424 (solid line) and LogNormal (dashed line) non-linear curve functions.
425

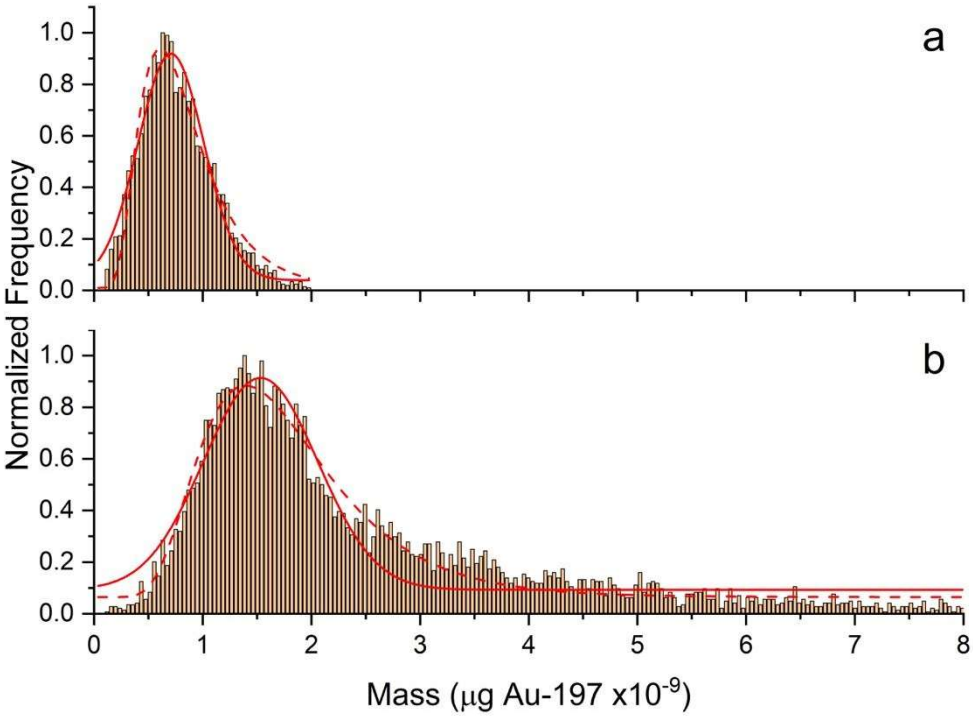

Figure 3. Particle mass distributions of a.) precursor Au-cit NPs and b.) Au-PS/PS-*b*-PAA CPs. Nanoparticle mass distributions were fitted to Gaussian (solid line) and LogNormal (dashed line) non-linear curve functions.

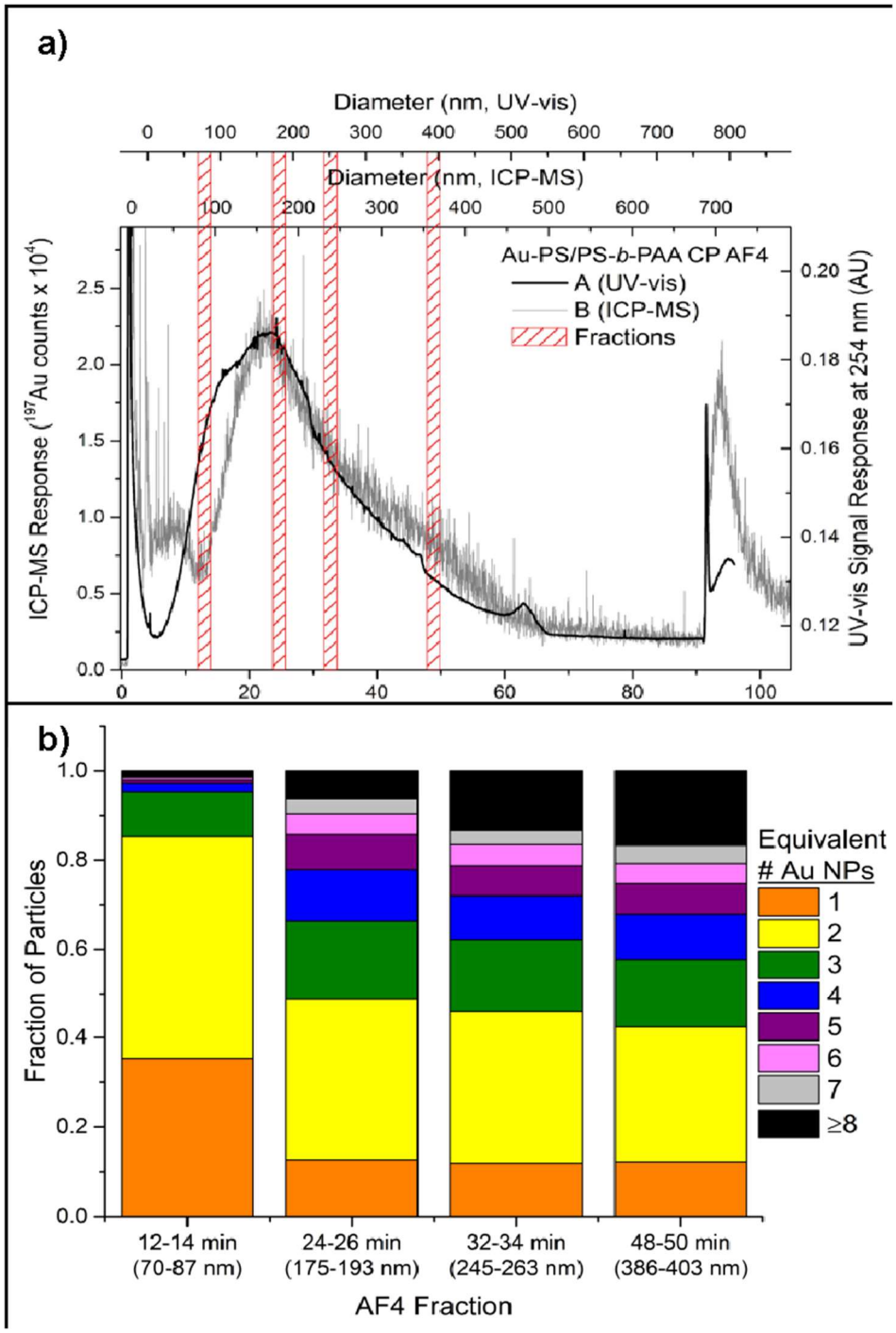

Figure 4. a.) Replicate AF4 separations of the Au-PS/PS-*b*-PAA CP using UV-vis detection (separation A) and ICP-MS (separation B). Four fractions (2 minutes each) were collected for spICP-MS analysis during separation A. The AF4-UV-vis signal is replicated well by the AF4-ICP-MS data. Differences in flow conditions resulted in a slightly different relationship between time and diameter for separation A and B. b) A simplified stacked bar histogram was produced from the spICP-MS data for each fraction.

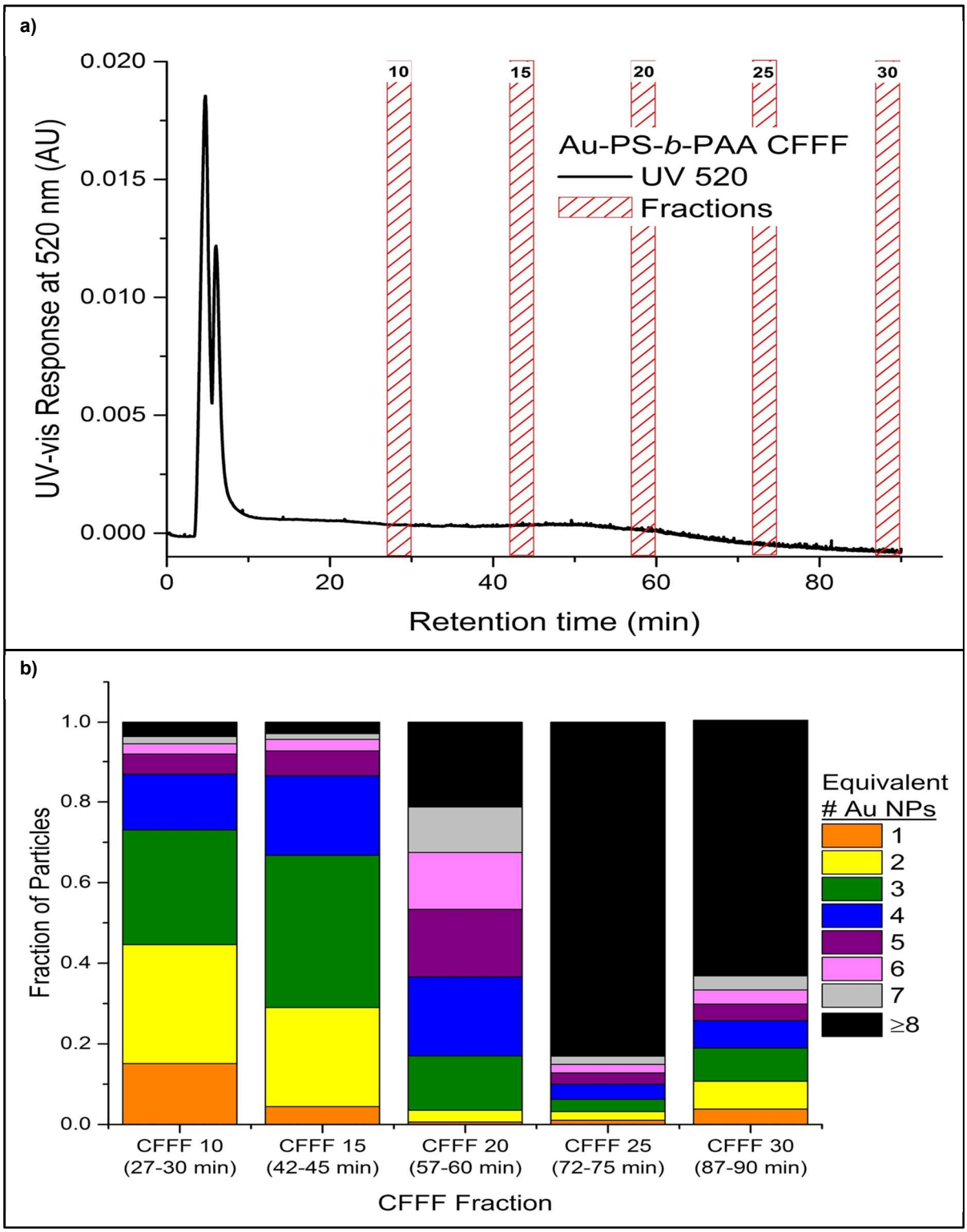

Figure 5. **a)** CFFF separation of the Au-PS/PS-*b*-PAA CP with UV-vis detection. Thirty fractions (3 minutes) were collected for spICP-MS analysis. **b)** A histogram of select fractions are shown to illustrate increase in incorporated Au mass with increasing retention time.

469